Magnetotelluric evidence for a melt-rich magmatic reservoir beneath Mayotte

Pierre Wawrzyniak, Fabrice Gaillard, Sophie Hautot, Joan Andújar, Pascal Tarits, Laurent Arbaret, Samuel Guegan, David Sifré, Jean-François D'eu, Jacques Deparis, et al.

Article

Magnetotelluric evidence for a melt-rich magmatic reservoir beneath Mayotte

https://doi.org/10.1038/s41586-025-09625-4

Received: 15 March 2024

Accepted: 12 September 2025

Published online: 29 October 2025

Check for updates

Pierre Wawrzyniak[1]✉, Fabrice Gaillard[2]✉, Sophie Hautot[3], Juan Andujar[2], Pascal Tarits[4], Laurent Arbaret[2], Samuel Guegan[2], David Sifré[2], Jean-François D'Eu[5], Jacques Deparis[1], Anne Lemoine[1], Isabelle Thinon[2], Sheldon Warden[6] & Frédéric Dubois[1]

The exact nature of crustal magmatic reservoirs is elusive as they cannot be sampled in situ. The traditional view that magma chambers contain essentially molten material has recently been replaced by the transcrustal magmatic system (TCMS), in which reservoirs are mostly composed of immobile magmatic crystals with a minute fraction of more mobile melt[1–3], creating a 'magmatic mush'[3]. Eruptions are possible if a significant portion of melt segregates into melt-rich lenses within the mush reservoir[1–3]. The TCMS concept is, however, a default model essentially justified by the absence of clear geophysical signatures of melt-rich magma chambers[1,4], and by the rare and tentative estimates of the melt fraction in the crustal storage zones based on geochemical and textural analysis of eruptive products[5,6]. Here we image a bright electrical conductor at 23 ± 1 km below sea level beneath Mayotte island that we interpret as a magmatic reservoir, based on laboratory measurements of Mayotte's melt conductivity. This large magmatic reservoir (more than 200 km^3) contains a high melt fraction (22–42%). Such a crystal-to-liquid ratio matches the reconstructed differentiation paths[7–9] producing the melts that recently erupted at Mayotte. This reservoir is possibly connected to the system that fed the large submarine eruption of Fani Maoré in 2018–2019[10].

Although most volcanic systems produce small-volume eruptions (<1 km^3), large volumes of magma are believed to be stored beneath these active centres[1,11]. However, geophysical exploration has rarely provided clear images of such magmatic regions[1]. In a thorough compilation, ref. 12 revealed that the seismic anomalies so far observed can be interpreted as magmatic zones with much less than 20% melt for volumes of 30 km^3 to 10^4 km^3. However, several points remain unclear, owing to long-recognized difficulties in (1) imaging relatively small (melt rich) magma systems[1,4,12] (that is, <100 km^3), and (2) quantifying melt fractions from seismic wave velocity data (V_P, V_S, V_P/V_S). In the absence of clear geophysical identification of magma chambers, and based on modelling of the thermomechanical properties of magmatic reservoirs[2], the transcrustal magmatic paradigm[1] has been proposed, in which melt batches are distributed diffusely at depth. This implies that the traditionally held concept[1] of magma chambers (that is, stagnant melt-rich regions) constitutes only a small part of the reservoir.

A powerful but less popular geophysical means of tracking melt in the crust is by magnetotelluric (MT) methods, which determine the vertical and lateral variation in electrical conductivity in Earth's interior[13]. The conductivity of melts is much higher than that of solids[4,14,15], making estimates of melt fraction using the conductivity of solid–melt mixtures relatively unambiguous, as long as the conductivity of both melt and solid are known[4]. Several MT studies have imaged magmatic reservoirs[15–19] and partial melt in the mantle[20]. In most cases, though, the attempts to quantify the melt fraction from the conductivity of these magmatic reservoirs have been imprecise because of the absence of constraints on the melt conductivity[16] and the impossibility of using predictive models of melt conductivity[21]. In the rare cases where melt conductivity is well known[4], the retrieved melt fractions are found to be low (for example, <10%). Here we combine thorough field and laboratory constraints to investigate a magmatic reservoir beneath Mayotte, France, in the Comoros archipelago.

Mayotte within the Comoros volcanic chains

The Comoros volcanic archipelago extends over 600 km long and 200 km wide[22] with a globally east–west orientation between East Africa and Madagascar in the north Mozambique channel (Fig. 1). It is composed of four main islands (Grande Comore, Mohéli, Anjouan and Mayotte, the oldest and easternmost). Submarine volcanic seamounts furthermore form major morphological ridges, as, for example, the East Mayotte volcanic chains[10], or are distributed in the great volcanic provinces[22] on the abyssal plain. The archipelago was built on a thick sedimentary cover[23] (2–3-km thick) and a Mesozoic oceanic crust[10]. The Comoros volcanism began in the Tertiary time (about 32 million years ago (Ma)) in the eastern part (Zélée-Geyser bank and Mayotte), then spread northwestwards from 8 Ma to 9 Ma to form the present-day archipelago[24]. Currently, two volcanoes are active, the Karthala Volcano

[1]BRGM, Bureau des Recherches Géologiques et Minières, Orléans, France. [2]Institut des Sciences de la Terre d'Orléans, CNRS-INSU/Université d'Orléans/BRGM, Orléans, France. [3]IMAGIR Sarl, Tech-Iroise, Saint Renan, France. [4]IUEM, Institut Universitaire Européen de la Mer, LGO, UMR 6538 - IUEM/UBO, Plouzané, France. [5]MAPPEM Geophysics SAS, Marine Electromagnetic Investigation, Batiment Tech-Iroise, Saint-Renan, France. [6]Hyperion Geophysical Service, Strasbourg, France. ✉e-mail: P.Wawrzyniak@brgm.fr; fabrice.gaillard@cnrs-orleans.fr

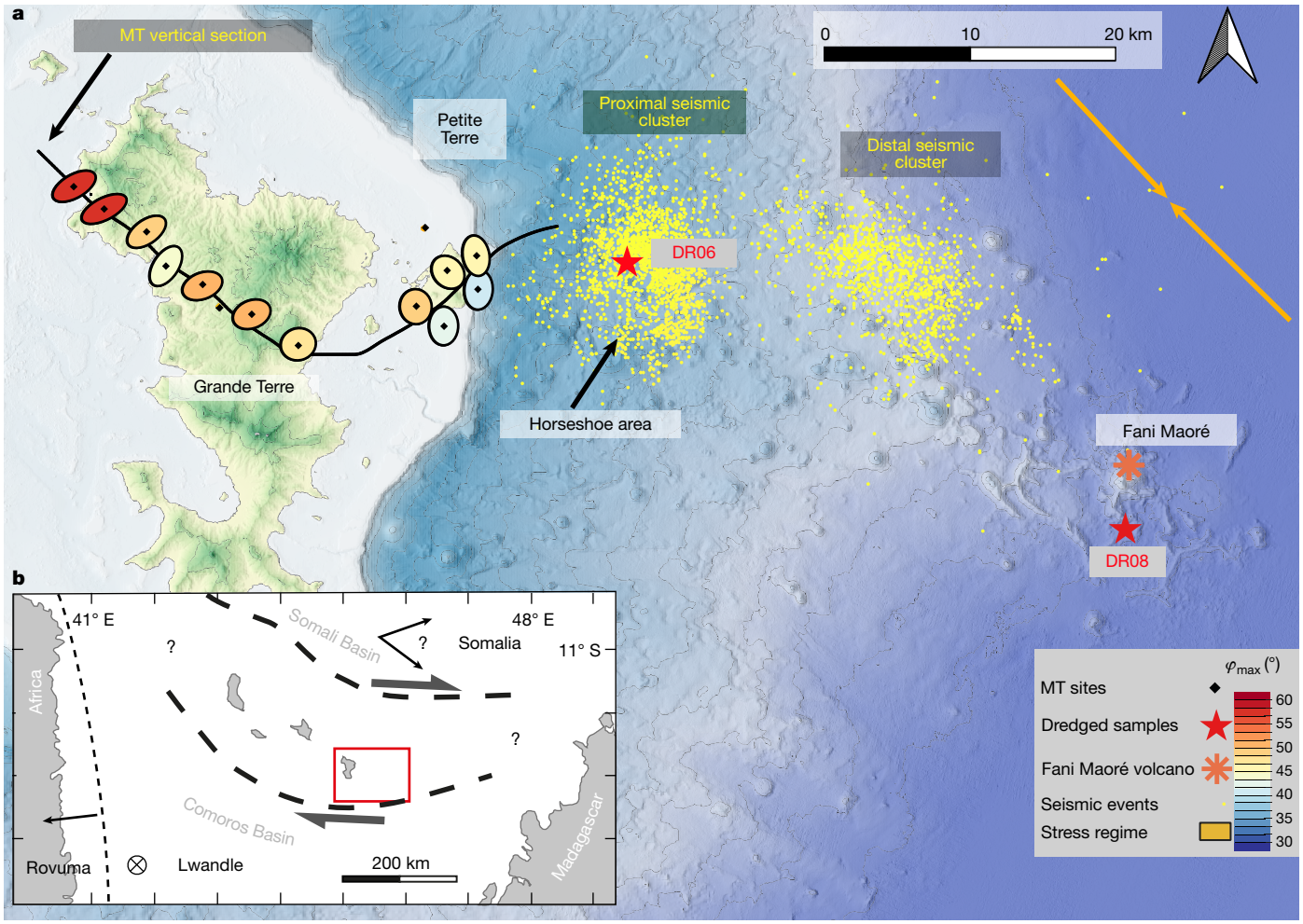

Fig. 1 | Map of the investigated area at Mayotte. a, Black diamonds are the shallow marine and onland MT sites on Mayotte used for this study, surrounded by a phase tensor ellipsis computed at a period of 100 s and filled with φ_{max} values (in degrees; values above 45° indicate a decrease in electrical resistivity below the depth of investigation, see colour scale in the key in the bottom-right corner). The black line indicates the vertical section in the 3D MT model shown in Fig. 3. The yellow circles indicate the epicentres of the June 2018–June 2020 seismic catalogue concatenated from refs. 33,34 (selection of seismic events detected from land array with magnitude >3 and root mean square <0.3 and ocean bottom seismometer (OBS) marine array used for velocity modelling), which shows proximal and distal clusters. The orange star is the submarine Fani Maoré volcano (2018–2021) and the red stars are samples DR06 and DR08 obtained from dredging during the MAYOBS2 survey[43] (Methods). The orange arrows are the regional stress field from ref. 32. **b**, Regional kinematics in the Mozambique Channel with plate boundaries and strike-slip regime[10,23,29,34]. The red rectangle represents the area shown in **a**. The black half arrows show the active strike-slip tectonic regime of the Comoros[29]. Lwandle plate tectonics is known; Somalia plate tectonics is still under debate.

in the western part of the Grande Comore island, and the submarine Fani Maoré volcano 50 km east of Mayotte. Mayotte is composed of two main islands, Grande Terre (west) and Petite Terre (east), separated by a lagoon. The subaerial volcanic activity initiated around 6.5 Ma (ref. 25) and the most recent activity was dated 4 thousand years ago[26,27]. The origin of volcanic activity in the Comoros is still a subject of debate, with two main theories[28,29]: (1) mantle plume interaction with the oceanic lithosphere[30,31]; and (2) deformation in the lithosphere triggered by Lwandle and Somalia plate[10,32] dynamics. Figure 1b shows the regional structural map marked by a right-lateral, 110° N-directed, shear zone[32].

Since 10 May 2018, Mayotte has been experiencing the biggest offshore seismo-volcanic crisis ever documented[10,28,33–36]. A new, 820-m-high submarine volcanic edifice (named Fani Maoré; Fig. 1) has been discovered[10], with an estimated erupted volume of >6.55 km^3 (ref. 37). In the period May 2018–May 2021, geophysical monitoring revealed telluric activity including (1) global eastwards displacement of 21–25 cm and a 10–19 cm subsidence of Mayotte[10,35], and (2) more than 100,000 earthquakes in 2 regions, located along a 22-to-45-km-deep proximal cluster centred on the active submarine 'horseshoe' volcanic area and a northwest–southeast distal cluster trending towards Fani Maoré[10,28,34–36] (Fig. 1). Two main interpretations[38] suggest either a 27-km-deep large-volume magma reservoir below the horseshoe area[34], or below Fani Maoré with an additional source below Mayotte island[28].

Mayotte's magma and their storage

The volcanism at Mayotte is alkaline[8,25,27], with a large range in differentiation index, from primitive mantle melts (for example, basanites) to strongly differentiated compositions (for example, phonolites). Figure 2 makes clear that the recent lavas found onshore and offshore constitute a single chemical evolution trend[7–9]. Recent petrological surveys have focused on offshore sampling and identified three types of melt composition[7–9]: putative parental basanite, evolved basanite and phonolite (Fig. 2). The parental basanite is most likely issued from melting of a lherzolitic mantle[8]. The production of evolved basanite liquids, which constituted most of the Fani Maoré eruptive event, implies crystallization of around 50% of the parental basanite[8] (Fig. 2). The phonolite melt can then be formed by the partial crystallization of the evolved basanite[7,9]. Thermobarometric investigations combined with thermodynamic modelling[8] suggest that the magmatic system

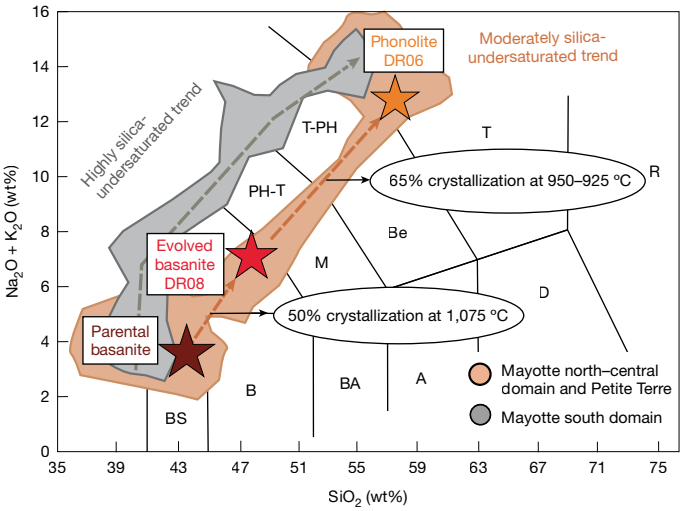

Fig. 2 | Chemical composition of lavas at Mayotte. Total alkali ($Na_2O + K_2O$) versus SiO_2 diagram illustrating the two compositional differentiation trends characteristic of Mayotte magmatism: highly silica undersaturated and moderately silica undersaturated[7,8,27]. We consider only the most recent eruptive products (from the north–central domain of Mayotte), that is, the moderately silica-undersaturated line. The stars show the parental basanite (brown), evolved basanite (red, DR08) and phonolite (orange, DR06) compositions described in this work. The degree of crystallization and temperatures necessary to produce evolved and phonolitic melts from their parental counterparts are indicated (see text and Methods). BS, basanite; B, basalt; BA, basalt-andesite; A, andesite; M, mugearite; Be, benmoreite; D, dacite; T, trachyte; R, rhyolite; T-PH, tephri-phonolite; PH-T, phono-tephrite.

feeding the Fani Maoré volcano is multi-levelled, involving the production of the parental basanite at >80 km depth, which rises from a deep reservoir (37–48 km in depth), in which the evolved basanite is produced by fractional crystallization. The evolved basanites then migrated to near-Moho depths (17 ± 6 km) before producing the Fani Maoré eruption. It should be noted, however, that there is a high level of uncertainty around the application of both thermobarometric methods and thermodynamic calculations to such alkaline magmas[7]. We thus conducted high-pressure–high-temperature experiments on the evolved basanite composition. These experiments show that the near-liquidus olivine–magnetite–glass phase assemblages of the evolved basanite can be reproduced at temperatures of 1,075 ± 10 °C and pressures ranging from 0.4 GPa to 0.65 GPa (Methods). This is equivalent to a depth of 13–25 km. The offshore phonolite liquids have mostly been found near the horseshoe area (Fig. 1). A range of production conditions have been suggested for these liquids: on the basis of thermobarometric analyses and thermodynamic modelling, ref. 9 proposed that they derive from the crystallization of the evolved basanite at 15–20 km, whereas ref. 7 constrained their formation at 7 ± 1 km using experimental phase equilibria. At such shallow depths, iron-rich phonolite melts (that is, 6–7 wt% FeO) are produced via crystallization of 65% of the evolved basanite at 925–950 °C (Methods). According to ref. 7, there is an onshore–offshore dichotomy for phonolite based on their iron content: iron-poor (4 wt% FeO) onshore phonolite is produced at greater depth, around >8 km, but no storage depths were firmly defined. To summarize these petrological constraints, evolved basanites are expected to be stored at mid-lithospheric depth (13–48 km), whereas phonolite melts are expected to be found at shallower levels (7 km for offshore occurrences, slightly deeper for onshore phonolites).

MT imaging beneath Mayotte

We conducted several MT surveys and imaged a large electrically conductive body beneath Mayotte which, combined with laboratory measurements, is interpreted in terms of magmatic storage. The technical details of the MT surveys and the laboratory measurements are provided in Methods.

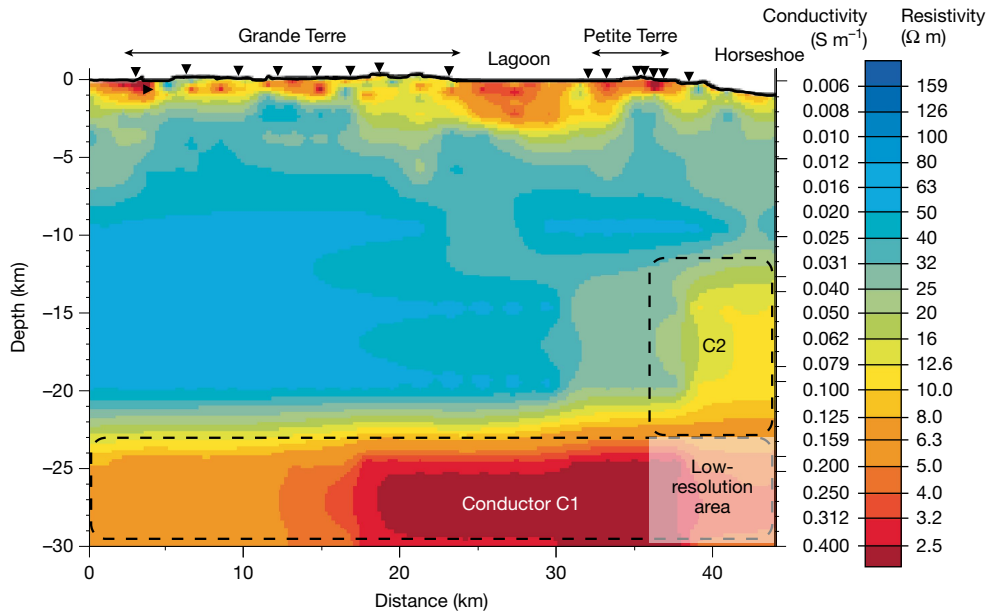

Fig. 3 | Vertical and lateral variations of electrical conductivity beneath Mayotte. The plot shows the vertical conductivity and resistivity section extracted from the 3D MT inversion results. This 30-km-deep electrical resistivity profile corresponds to the northwest–southeast + southwest–northeast broken black line shown in Fig. 1. The black triangles show the orthogonal projection of the MT stations on the profile. The conductivity and resistivity scale is upper- and lower-bounded by the maximum and minimum values retrieved from the inversion procedure. Two conductive bodies named C1 and C2 are outlined with dotted black lines and are interpreted in terms of magmatic storage. C2 maximum conductivity is located under the Horseshoe area. The C2 westwards boundary is defined by a 25 Ω m isoresistivity lateral contrast corresponding to a melt fraction of 7%. Below C2, a low-resolution area is shown in the eastern part of the profile.

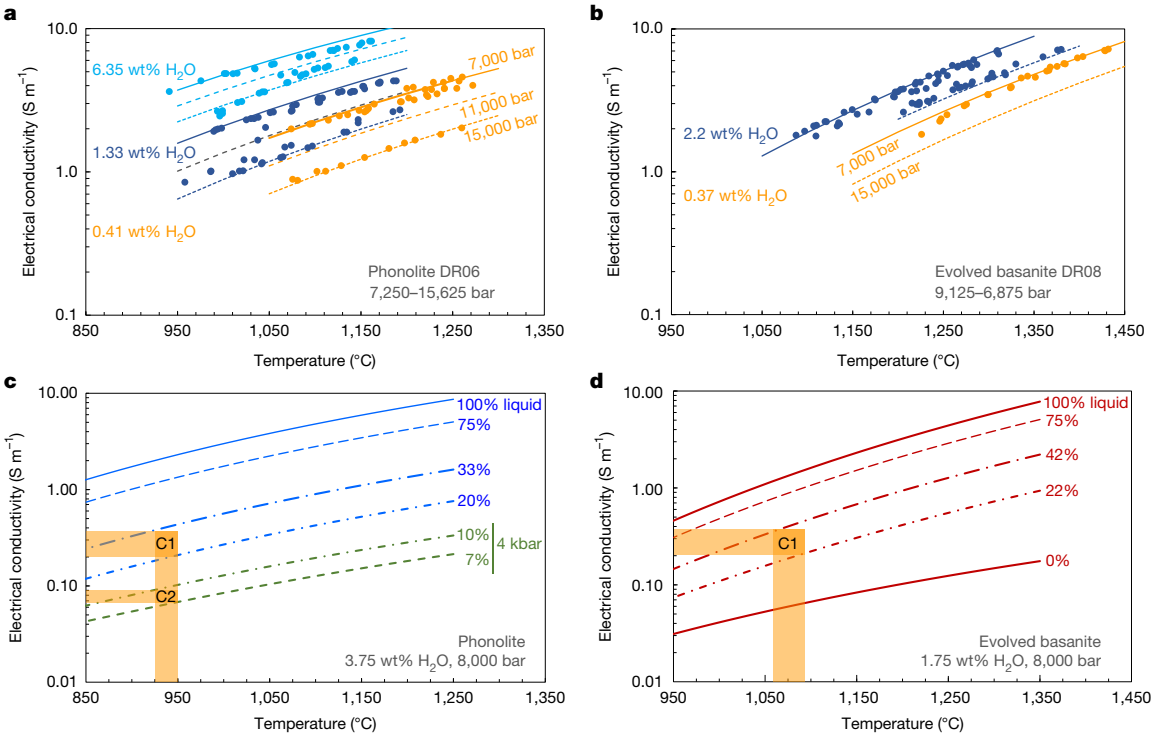

Fig. 4 | Electrical conductivity of Mayotte's melts and magmas. Laboratory data on alkaline melt conductivities are used to interpret the nature of the C1 and C2 magmatic reservoirs beneath Mayotte. **a**,**b**, Laboratory measurements of electrical conductivities of phonolite (DR06; **a**) and evolved basanite (DR08; **b**) melts as a function of temperature. It is noted that the investigated melts contain various water contents (0.41 wt% to 6.35 wt% for phonolite and 0.37 wt% to 2.2 wt% for evolved basanite) and are subjected to a range of pressure conditions (**a**, 0.7 GPa, 1.1 GPa and 1.5 GPa; **b**, 0.7 GPa and 1.5 GPa). The solid and dashed lines are mathematical models (Methods) describing the effects of temperature, at the labelled pressure, and for the melt water contents similar to the labelled values. These curves are issued from a global fit to the entire dataset (Methods). The colour code indicates the melt water contents for both experimental datapoints and calculated curves. **c**,**d**, The effects of temperature and melt contents (expressed in vol%) on the electrical conductivity of Mayotte's magma (melt + crystals; Methods), and these magma conductivities compared with the C1 and C2 conductors (horizontal bands; see Methods for the width). Phonolite (**c**) and evolved basanite (**d**) are modelled, with melt water contents of 3.5 wt% and 1.75 wt%, respectively. The conductivity of the solid in **c** is 0.01 S m^{-1} (Methods), and a line, labelled 0%, directly shows the conductivity of a melt-free clinopyroxene–olivine assemblage versus temperature in **d**. The vertical bands indicate the temperature conditions determined by petrological survey[7–9] for the production of phonolite and evolved basanite liquids. These liquids are similar to the eruptive products recently dredged at Mayotte[8].

Figure 3 shows the vertical and lateral variations in electrical conductivity (and resistivity) beneath Mayotte. The vertical section combines 2 slices of a 30-km-deep three-dimensional (3D) MT inversion model (Methods). The first 5 km beneath Mayotte (Petite Terre and Grande Terre islands) has conductivity higher than 0.04 S m^{-1} and shows lateral heterogeneity. Beneath Grande Terre, we found a resistive area (conductivity approximately 0.02 S m^{-1}) in the 5–23 km depth range. At 23 km in depth, the top of a conductive body (conductivity >0.2 S m^{-1}), here named C1, was encountered. Under the eastern part of Petite Terre, the resistive area is in the depth range 5–12 km. Between 12 km and 23 km depth on the eastern side of Petite Terre, there is a 0.04–0.125 S m^{-1} conductor named C2 (>0.083 S mm^{-1} on the eastern part). The C1 conductor is also present beneath C2. We performed different sensitivity tests on C1 and C2: (1) the top of C1 is located at between 22 km and 24 km depth, and its conductivity ranges from 0.2 S m^{-1} to 0.33 S m^{-1}, and (2) C2 is also well constrained by the dataset (see Methods for details).

The two electrical discontinuities seen at 4 km and 23 km in depth are consistent with seismic studies conducted on land. Reference 39 revealed a Vs discontinuity (increasing with depth) at 4 km, interpreted as being the base of the island. Reference 34 indicated an increase in V_P/V_S ratios at 22 km beneath Mayotte. Offshore passive seismic tomography[40] showed a low-velocity zone (high V_P/V_S ratio) in the depth range 20–30 km, below the Horseshoe volcanic area, which was interpreted as a mushy magmatic body. High V_P/V_S ratios combined with high conductivity (Fig. 3) are compatible with the presence of a magmatic body beneath the island that most likely extends towards the Horseshoe domain.

We exclude the possibility that both C1 and C2 are hydrothermal systems because of the great depth (12–30 km) and the relatively dry nature of the magma, precluding the presence of voluminous deep water-rich fluids. C1 and C2 clearly represent magmatic storage zones, but constraints on the conductivity of the alkaline Mayotte melts are required to define this storage in terms of conditions.

Deciphering Mayotte's plumbing system

Figure 4a,b shows the laboratory measurements of electrical conductivity versus temperature for phonolite (sample DR06) and evolved basanite liquids (DR08) containing different water contents and subjected to different pressures. We used the four-wire experimental protocol defined by ref. 41. Increasing water content and temperature significantly increases the melt conductivity, whereas increasing pressure has the opposite effect. The conductivity of phonolite and evolved basanite liquids have been parameterized against pressure–temperature–H_2O using a modified Arrhenius formalism[4,41]. This parameterization allows us to calculate the conductivity of the Mayotte melts and magma (that is, melt + crystal) for a range of temperature, pressure, water contents and crystal fractions (Methods). The parameterization reproduces the experimentally measured conductivities to within 5%.

Figure 4c,d compares the conductivity values of C1 and C2 with the electrical conductivity of the Mayotte phonolite and evolved basanite

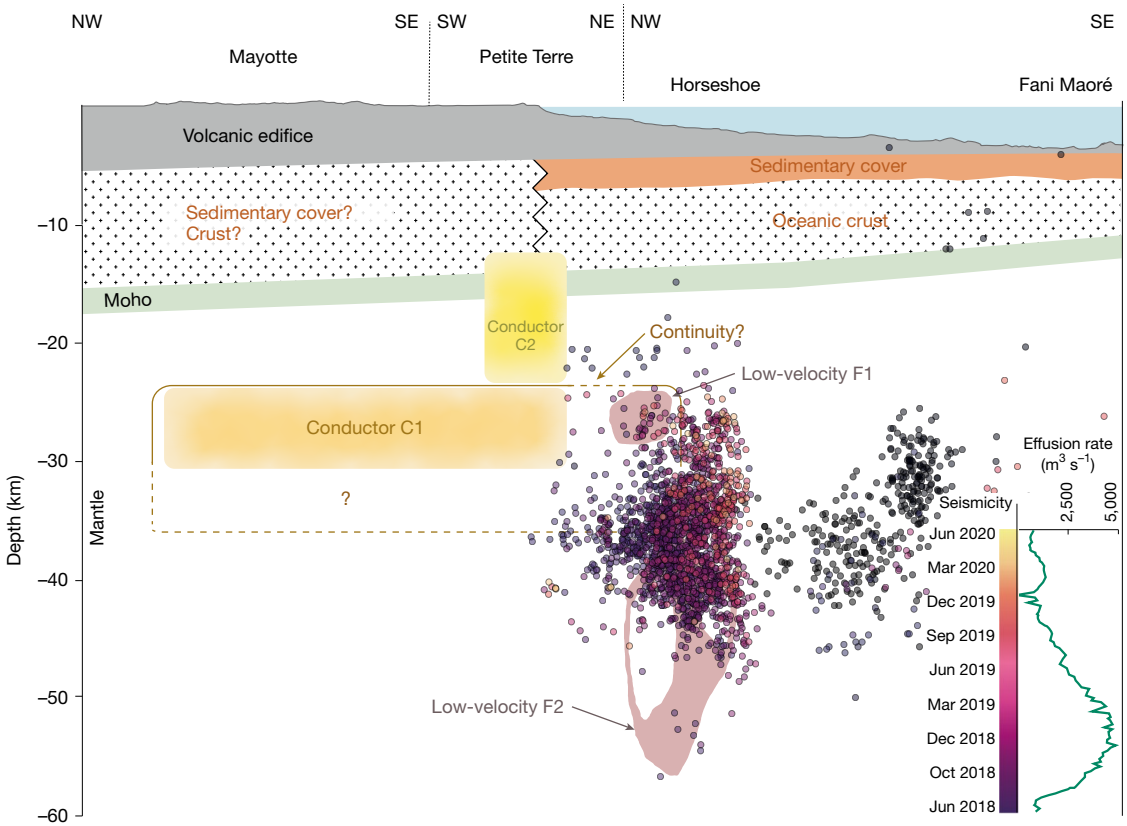

Fig. 5 | Interpretative structural scheme of the Mayotte volcanic plumbing system. This interpretation is inferred by joint experimental petrophysics and MT data (this study, conductors C1 and C2) and by passive seismic tomography[40] (low-velocity zones F1 and F2). The June 2018–June 2020 seismic catalogue concatenated from refs. 33,34 is shown as unscaled coloured dots with a temporal colour scale, linked to effusion rate chronicles (bottom-right curve). MT data revealed a magmatic mush hosting 22–42% of evolved basanite melt (conductor C1) at 25 km below Mayotte and, just above, a shallower reservoir hosting 7–10% of phonolitic melt (conductor C2) below Petite Terre. We suggest a continuity between the C1 and C2 conductor and the low-velocity structure named F1. The Fani Maoré volcano is composed of evolved basanite and is shown in grey on the eastern seafloor part. Vertical and horizontal scales are identical.

liquids for a range of magmatic conditions. The dissolved water contents in the melts are 1.75 wt% and 3.5 wt%, which agrees with literature estimations for the evolved basanite and phonolite melts, respectively[7–9] (see also our own assessment in Methods). The pressure conditions correspond to the depth of the C1 and C2 conductors, that is, 800 MPa and 400 MPa (8,000–4,000 bar), respectively. The conductivity of both melts exceeds the conductivity of C1 and C2 by a factor two to three. We assume below that the conductivity difference can be ascribed to the presence of magmatic crystals in the reservoirs, which are less conductive (Methods). We first discuss C1 in relation to the evolved basanite case. Considering a temperature of 1,075 ± 10 °C for the production of this melt, the conductivity of C1 is consistent with a reservoir containing 22–42% evolved basanite liquid plus 78–58% crystals (Fig. 4d). Following ref. 8, the crystals are here assumed to be a 1:4 mixture of olivine and clinopyroxene (Methods). Such a range of crystal fractions estimated from the conductivity of C1 is higher but comparable to the 50% crystallization estimated by petrological methods[8] to produce an evolved basanite liquid from a parental basanite. The impact of uncertainty in the storage temperature for the evolved basanite is represented in Fig. 4d, which also shows the uncertainty in C1 conductivity; both uncertainties are already considered in the assessed range of melt (22–42%) and crystal (78–58%) contents in C1. Uncertainties in the melt water content of ±0.5 wt% would translate into a minimum of 18% (for 2.25 wt% H_2O) and a maximum of 47% (for 1.25 wt% H_2O) of melt required to account for the electrical conductivity of C1. The assessment of melt fraction in the C1 conductor is thus a robust feature, which is furthermore broadly consistent with independent petrological estimations.

Using a similar methodology, we can relate C1 to a phonolite case. Considering a temperature of 925–950 °C for the production of phonolite liquid[7], we deduce that C1 conductivity is consistent with a reservoir containing 20–33% of phonolite melt, that is, 80–67% of crystals (Fig. 4c). We assume a conductivity for the crystals of 0.01 S m^{-1} (Methods). This range of crystal fraction is very close to the degree of crystallization required to transition from an evolved basanite to a phonolite melt according to the petrological data[7,9]. Yet, ref. 7 demonstrated that such phonolite melts must be produced at depth much shallower than C1. Thus, although the phonolite case could match the conductivity of C1, existing phase equilibria constraints do not favour this scenario.

We therefore endorse the scenario in which C1 is a reservoir containing 22–42% of evolved basanite liquid plus 78–58% crystals. The C1 reservoir thus contains a greater solid fraction than (50%) expected for the production of evolved basanite melt from parental basanite. This possibly suggests that the magmatic reservoir has inherited crystal cumulates from previous and long-term replenishment–differentiation iterations. This is in line with the transcrustal magmatic system paradigm[1]. Yet, we infer a fairly high melt fraction, particularly in view of the large conductive volume (most likely >200 km^3), which is not usual in transcrustal models. Alternatively, we could argue that the C1 conductivity is an average that includes some wall-rocks in addition to the magmatic reservoir, that is, a sort of composite permeable network. In this case, the reservoir may include local pockets of much greater melt fraction. At this stage, however, it is not possible for us to image conductivity heterogeneities and consequently melt

fraction variations within C1. C1 shows a well resolved but uniform conductivity of 0.2–0.33 S m^{-1} (Methods).

C2 is first discussed in the framework of an evolved basanite scenario. At 1,075 °C and 0.4 GPa pressure, 0–13% of melt is required to match the C2 conductivity range (0.04 S m^{-1} to 0.125 S m^{-1}). Yet, such a highly solidified magmatic reservoir should, according to phase equilibria principles, be cooler than C1, and thus host a much more differentiated residual melt, that is, a phonolitic melt. C2 is indeed located at a depth that better matches onshore and offshore phonolite melt production regions[7,9]. In such a context, the C2 conductor can be explained by a magmatic system containing 7–10% phonolite melt (at 0.4 GPa), with 3.5 wt% dissolved H_2O, at 925–950 °C (Fig. 4c). A cooler phonolite system would involve a higher melt fraction as can be read on Fig. 4c. Considering phonolite melts with 4 wt% H_2O instead of 3.5 wt% would imply an upper range of melt content of 9% instead of 10%, which marginally affects our conclusion. Finally, changing the conductivity of the solids from 0.01 S m^{-1} to 0.001 S m^{-1} modestly changes the retrieved melt fractions (from 10% to 11% for the upper bound). The interpretation of the C2 in terms of melt fraction is thus a robust feature. It is difficult to discuss the nature of C2 in more detail at this point as it occurs at the margin of our MT array coverage (see the sensitivity analysis of C2 in Methods and Fig. 5). However, it is important to carry out further investigation on the eastern extension of this body as it seems to extend towards the Horseshoe domain, where the recent seismicity[33,34] and phonolitic volcanism[9] have been observed. There is probably a connection between the C2 conductor and the volcano-seismic activity at the Horseshoe, which deserves further investigation (Fig. 5).

Possible hybrid onshore–offshore plumbing system

Finally, we consider whether there is any connection between the large C1 magmatic reservoir and the gigantic Fani Maoré eruption. We produced Fig. 5 to illustrate the discussion on this complex question. The seismicity recorded during the Fani Maoré eruptive event initiated much deeper, that is, 40 km, and 30 km eastwards of C1[33,34]. However, the seismicity accompanying the largest portion of the drainage within the putative reservoir (that is, late 2018 to early 2019) is located next to C1[33]. As illustrated in Fig. 5, C1 is located at the same depth as a mush (corresponding to a low-velocity volume, named F1 in Fig. 5) revealed by passive seismic tomography[40], 15 km eastwards, on the seawards side. This suggests a continuity of the magmatic structures imaged using the MT data (this study) and by seismic tomography[40] extending from beneath Mayotte island to beneath the Horseshoe system. Figure 5 allows a visualization of this scenario. Yet, the absence of offshore MT data and onshore 3D seismic tomography prevents us from establishing a firm link between these deep magmatic structures. We believe that claiming a firm connection between the C1 reservoir and the new volcano formed in 2018–2019 at Fani Maoré would be at this stage premature, but it can definitively not be excluded. We furthermore note that a recent thermomechanical model[42] of the Fani Maoré eruption rates require the involvement of a magmatic mush, large enough to supply the large magma flow rate during the eruptive climax. The C1 conductor might constitute a part of such a reservoir. Defining its lateral extension beneath the island and towards the sea is thus an urgent research action to undertake.

Online content

Any methods, additional references, Nature Portfolio reporting summaries, source data, extended data, supplementary information, acknowledgements, peer review information; details of author contributions and competing interests; and statements of data and code availability are available at https://doi.org/10.1038/s41586-025-09625-4.

1. Cashman, K. V., Sparks, R. S. J. & Blundy, J. D. Vertically extensive and unstable magmatic systems: a unified view of igneous processes. *Science* **355**, eaag3055 (2017).
2. Bachmann, O. & Bergantz, G. W. Deciphering magma chamber dynamics from styles of compositional zoning in large silicic ash flow sheets. *Rev. Mineral. Geochem.* **69**, 651–674 (2008).
3. Cooper, K. M. & Kent, A. J. Rapid remobilization of magmatic crystals kept in cold storage. *Nature* **506**, 480–483 (2014).
4. Laumonier, M., Gaillard, F., Muir, D., Blundy, J. & Unsworth, M. Giant magmatic water reservoirs at mid-crustal depth inferred from electrical conductivity and the growth of the continental crust. *Earth Planet. Sci. Lett.* **457**, 173–180 (2017).
5. Holness, M. B., Stock, M. J. & Geist, D. Magma chambers versus mush zones: constraining the architecture of sub-volcanic plumbing systems from microstructural analysis of crystalline enclaves. *Philos. Trans. R. Soc. A* **377**, 20180006 (2019).
6. Weber, G., Caricchi, L., Arce, J. L. & Schmitt, A. K. Determining the current size and state of subvolcanic magma reservoirs. *Nat. Commun.* **11**, 5477 (2020).
7. Andújar, J. et al. Experimental evidence for the shallow production of phonolitic magmas at Mayotte. *C. R. Geosci.* **354**, 225–256 (2023).
8. Berthod, C. et al. The 2018-ongoing Mayotte submarine eruption: magma migration imaged by petrological monitoring. *Earth Planet. Sci. Lett.* **571**, 117085 (2021).
9. Berthod, C. et al. Mantle xenolith-bearing phonolites and basanites feed the active volcanic ridge of Mayotte (Comoros archipelago, SW Indian Ocean). *Contrib. Mineral. Petrol.* **176**, 75 (2021).
10. Feuillet, N. et al. Birth of a large volcanic edifice offshore Mayotte via lithosphere-scale dyke intrusion. *Nat. Geosci.* **14**, 787–795 (2021).
11. White, S. M., Crisp, J. A. & Spera, F. J. Long-term volumetric eruption rates and magma budgets. *Geochem. Geophys. Geosystems* **7**, 2005GC001002 (2006).
12. Paulatto, M. et al. Advances in seismic imaging of magma and crystal mush. *Front. Earth Sci.* **10**, 970131 (2022).
13. Chave, A. D. & Jones, A. G. *The Magnetotelluric Method: Theory and Practice* (Cambridge Univ. Press, 2012).
14. Yoshino, T. in *Magmas Under Pressure* (eds Kono, Y. & Sanloup, C.) 281–319 (Elsevier, 2018).
15. Johnson, N. E. et al. Magma imaged magnetotellurically beneath an active and an inactive magmatic segment in Afar, Ethiopia. *Geol. Soc. Lond. Spec. Publ.* **420**, 105–125 (2016).
16. Hill, G. J. et al. Trans-crustal structural control of CO_2-rich extensional magmatic systems revealed at Mount Erebus Antarctica. *Nat. Commun.* **13**, 2989 (2022).
17. Comeau, M. J., Unsworth, M. J. & Cordell, D. New constraints on the magma distribution and composition beneath Volcán Uturuncu and the southern Bolivian Altiplano from magnetotelluric data. *Geosphere* **12**, 1391–1421 (2016).
18. Ichiki, M. et al. Magma reservoir beneath Azumayama Volcano, NE Japan, as inferred from a three-dimensional electrical resistivity model explored by means of magnetotelluric method. *Earth Planets Space* **73**, 150 (2021).
19. Isaia, R. et al. 3D magnetotelluric imaging of a transcrustal magma system beneath the Campi Flegrei caldera, southern Italy. *Commun. Earth Environ.* **6**, 213 (2025).
20. Key, K., Constable, S., Liu, L. & Pommier, A. Electrical image of passive mantle upwelling beneath the northern East Pacific Rise. *Nature* **495**, 499–502 (2013).
21. Pommier, A. & Le-Trong, E. "SIGMELTS": a web portal for electrical conductivity calculations in geosciences. *Comput. Geosci.* **37**, 1450–1459 (2011).
22. Thinon, I. et al. Volcanism and tectonics unveiled in the Comoros archipelago between Africa and Madagascar. *C. R. Geosci.* **354**, 7–34 (2022).
23. Masquelet, C. et al. Intra-oceanic emplacement of the Comoros archipelago through inherited fracture zones. *Tectonophysics* **882**, 230348 (2024).
24. Rusquet, A. et al. Phases of magmatism and tectonics along the Madagascar–Comoros volcanic chain, and synchronous changes in the kinematics of the Lwandle and Somalia plates. *J. Geophys. Res. Solid Earth* **130**, e2024JB029488 (2025).
25. Lacombe, T. et al. Late Quaternary explosive phonolitic volcanism of Petite-Terre (Mayotte, Western Indian Ocean). *Bull. Volcanol.* **86**, 11 (2024).
26. Nehlig, P. et al. Notice explicative, carte géologique France (1/30 000), feuille Mayotte (1179). Carte géologique par Lacquement, F., Nehlig, P. & Bernard, J. (BRGM Editions, Service géologique national, Orléans, 2013).
27. Pelleter, A.-A. et al. Melilite-bearing lavas in Mayotte (France): an insight into the mantle source below the Comores. *Lithos* **208**, 281–297 (2014).
28. Lemoine, A. et al. The 2018–2019 seismo-volcanic crisis east of Mayotte, Comoros islands: seismicity and ground deformation markers of an exceptional submarine eruption. *Geophys. J. Int.* **223**, 22–44 (2020).
29. Michon, L., Famin, V. & Quidelleur, X. Evolution of the East African Rift System from trap-scale to plate-scale rifting. *Earth Sci. Rev.* **231**, 104089 (2022).
30. Class, C., Goldstein, S. L., Stute, M., Kurz, M. D. & Schlosser, P. Grand Comore Island: a well-constrained "low $^3He/^4He$" mantle plume. *Earth Planet. Sci. Lett.* **233**, 391–409 (2005).
31. Chauvel, C. et al. Fani Maoré, a new "young HIMU" volcano with extreme geochemistry. *Earth Planet. Sci. Lett.* **626**, 118529 (2024).
32. Famin, V., Michon, L. & Bourhane, A. The Comoros archipelago: a right-lateral transform boundary between the Somalia and Lwandle plates. *Tectonophysics* **789**, 228539 (2020).
33. Mercury, N. et al. Onset of a submarine eruption east of Mayotte, Comoros archipelago: the first ten months seismicity of the seismo-volcanic sequence (2018–2019). *C. R. Geosci.* **354**, 105–136 (2022).
34. Lavayssière, A. et al. A new 1D velocity model and absolute locations image the Mayotte seismo-volcanic region. *J. Volcanol. Geotherm. Res.* **421**, 107440 (2022).
35. REVOSIMA *Bulletin de Mai 2023 de l'activité sismo-volcanique à Mayotte* (IPGP, Université de Paris, OVPF, BRGM, Ifremer, CNRS, 2023); https://www.ipgp.fr/wp-content/uploads/2023/06/Revosima_bull_20230606.pdf.
36. Cesca, S. et al. Drainage of a deep magma reservoir near Mayotte inferred from seismicity and deformation. *Nat. Geosci.* **13**, 87–93 (2020).
37. Berthod, C. et al. Temporal magmatic evolution of the Fani Maoré submarine eruption 50 km east of Mayotte revealed by in situ sampling and petrological monitoring. *C. R. Geosci.* **354**, 195–223 (2022).

38. Jacques, E. et al. Ring faulting and piston collapse in the mantle sustained the largest submarine eruption ever documented. *Earth Planet. Sci. Lett.* **647**, 119026 (2024).
39. Dofal, A., Fontaine, F. R., Michon, L., Barruol, G. & Tkalčić, H. Nature of the crust beneath the islands of the Mozambique Channel: constraints from receiver functions. *J. Afr. Earth. Sci.* **184**, 104379 (2021).
40. Foix, O. et al. Offshore Mayotte volcanic plumbing revealed by local passive tomography. *J. Volcanol. Geotherm. Res.* **420**, 107395 (2021).
41. Sifré, D. et al. Electrical conductivity during incipient melting in the oceanic low-velocity zone. *Nature* **509**, 81–85 (2014).
42. Mittal, T., Jordan, J. S., Retailleau, L., Beauducel, F. & Peltier, A. Mayotte 2018 eruption likely sourced from a magmatic mush. *Earth Planet. Sci. Lett.* **590**, 117566 (2022).
43. Jorry, S. *MAYOBS2 French Oceanographic Cruise, RV Marion Dufresne* SISMER Database (French Oceanographic Fleet, 2019).

Methods

MT imaging

MT dataset. In May 2019, a set of two land MT stations (002 and 003, Extended Data Fig. 1) and four marine MT stations (m01, m02, m03 and m04; Extended Data Fig. 1) were deployed around Petite Terre island for the purposes of geothermal exploration[44].

We conducted a second survey between 1 and 8 July 2020, to characterize the deep magmatic structures of Mayotte. We set up seven MT stations (n01, n03, n04, n05, n06, n07 and n08 with same characteristics as 2019 but with a combination of MFS06 and MFS07 magnetic coils) on Grande Terre along a north-northwest–south-southeast profile for 3–4 days of data acquisition at 512 Hz and 1 hour at 4,096 Hz.

In December 2020, we installed a third monitoring station at Dzaoudzi airport (203; Extended Data Fig. 1), near the landing strip, and acquired 4 days of data. Consequently, the MT dataset is composed of 15 stations: 3 permanent land stations, 8 land stations and 4 shallow marine stations.

All MT data are available at https://doi.org/10.18144/605e087b-74a7-4c3b-b733-a5e6167bea0a (ref. 45).

MT data processing. See the data repository at https://doi.org/10.18144/605e087b-74a7-4c3b-b733-a5e6167bea0a (ref. 45).

We processed the dataset using two-stage bounded influence remote reference processing through two codes: Birrp[46] and Razorback[47]. Both algorithms furnished similar MT impedance transfer functions but the Birrp results were of superior phase quality in the dead band (0.05–0.5 Hz). We used multiple remote references to reduce the noise impact on transfer function estimates. We obtained 15 MT 'broadband' soundings (10^{-2}–10^{3} s; Extended Data Figs. 2 and 3). The 2019 marine soundings m01, m02, m03 and m04 have lower signal-to-noise ratios owing to swell and larger error bars on antidiagonal components.

Three-dimensional inversion. We performed 3D inversions using the MININ3D code[48–51]. As the inversion grid parameterization for the inversion technique must be adapted to the properties and quality of the MT dataset, we adjusted the number of parameters (that is, horizontal and vertical distribution of cells) to the number and distribution of data. This approach led to the actual resolution of the data and produced a realistic blocky distribution of parameters (for example, ref. 50).

Given the non-homogeneous distribution of sites, we designed a specific grid of 26 × 33 × 18 cells, which included the bathymetry of the study area. The total volume of the 3D model was 508,000 km^3. The horizontal dimensions of the cells in the central part of the model was 1 × 1 km. The thickness of the layers ranges between 15 m and 25 km. The 3D part of the model overlays a stratified model below 25 km in depth with 2 layers of thickness 50 km making the full model (3D and 1D) 125-km thick over a homogeneous half space. The resistivity of the stratified deep layers was also included in the inversion. Seawater holds a fixed resistivity of 0.3 Ω m. The starting model was homogeneous.

The 3D inversion minimized a misfit function between the observed data (the four components of the impedance) and the 3D model response at all sites and frequencies weighted by the data variance. The regularization term is the variance of the distribution of resistivity across the whole model[48,49]. After a careful editing of the data for consistency and quality plus several tests of starting homogeneous resistivity value and error floor values, an optimum 10 Ω m was chosen as starting resistivity value, 3% error floor for the off diagonal and 10% for the diagonal impedances. For the final run, the starting root mean square of the misfit was 14.4 and decreased to 1.7. The data retained for the inversion and the model responses are shown in Extended Data Figs. 2 and 3. We show the results along an inflected line, composed of two slices (Fig. 1), including the Grande Terre 2020 survey and Petite Terre (Fig. 3). At site positions, we showed phase tensors computed at 100 s. The latter show maximum phases (φ_{max}) above 45°, indicating the presence of a conductor below the depth of investigation. In addition, at 100 s again, half of the sites show skew angles β above 3° (criterion after ref. 52), demonstrating the 3D dimensionality of the dataset. Moreover, ref. 44 already exhibited 1,000-s phase tensors for sites REM and 002 and evidenced their orthogonality with the regional oceanic ridge (around 135° N). The same trend is shown for 10 of the 14 stations in Extended Data Fig. 4.

Consequently, 3D inversion was necessary because of the geometry of the data distribution and the heterogeneity of the substratum. However, as the data are mostly along the profile line, they do not resolve well the structures away from the inflected line (Fig. 1). Hence, we presented the model in Fig. 3 only as a vertical slice along the oblique profile.

Sensitivity study. As the C1 and C2 conductors are key elements for understanding the magmatic system below Mayotte, we performed different sensitivity tests. The purpose of these tests is to determine whether changes in some of the key characteristics of the model were actually resolved by the data. We changed one parameter at a time, computed the responses for the modified models and compared the total misfit obtained at all sites to the misfit of our preferred model, expressed as a percentage of change of the misfit. First, we tested the depth to the top of conductor C1 between depths of 15 km and 30 km (Extended Data Fig. 5a). We obtained the minimum misfit variation between the forward model and real data for a top between 22 km and 24 km depth. Second, the layer containing the conductor C1 (Fig. 3) was set to be homogeneous in the 3D model. We tested different resistivity values between 1 Ω m and 15 Ω m (Extended Data Fig. 5b) and obtained best misfit values in the resistivity range 3–5 Ω m (that is, 0.2 S m^{-1} to 0.33 S m^{-1} in conductivity). Below and above these values, the misfit grows rapidly with the change in resistivity. Consequently, both top depth and resistivity of C1 are well constrained by the dataset.

Models cells within C1 are 10 × 10 × 15 km and C1 tops at 22 km depth. Thus, lateral resistivity variations within the 3–5 Ω m range, below 22 km and in the east–west direction under Mayotte island are poorly constrained by the dataset.

Finally, we tested the resolution of conductor C2. This body is mostly controlled by the Petite Terre data and was already present in the results of ref. 44. First, the whole 12–23 km layer (Fig. 3) was set to be homogeneous with a median value of 21 Ω m (computed for the whole heterogeneous layer) and the misfit increase was 9.9%. Then, C2 was replaced by a 50 Ω m block. The misfit increased by 18%. Finally, the resistive area west of C2 was set to be conductive with a conductivity value of 4 Ω m. The misfit increased by 35%. These 3 scenarios refute the hypothesis of a one-dimensional layer in the 12–23 km depth section and confirm that the dataset constrains the lateral transition between the resistor and C2 in Fig. 3. For the C2 body, the mean resistivity value is about 9 Ω m with a maximum value of about 10–12 Ω m, above which the misfit increases rapidly. Below about 7–8 Ω m, the misfit increases even more rapidly.

We also produced maps of misfit over the area of the MT survey (Extended Data Figs. 6 and 7) for depth and resistivity boundaries tested in the sensitivity analysis (Extended Data Fig. 5). These maps show the relative misfit changes (with respect to our best model misfit shown in Fig. 3) for the C1 conductor depth and resistivity. We show the misfit variations at the roof of C1 between 15 km and 30 km depth (Extended Data Fig. 6a,b, respectively) and the misfit for the resistivity of C1 between 1 Ω m and 15 Ω m (Extended Data Fig. 7a,b).

Deepening C1 to 30 km depth increases the misfit at most stations except station n05 (Extended Data Fig. 6, bottom) and slightly at the two northernmost marine stations off Petite Terre. Increasing C1 to 15 km depth increases the misfits in all stations located in Grande Terre (Extended Data Fig. 6, top) and slightly decreases the misfit of 2 marine sites (m04 and m02) around Petite Terre.

At a fixed roof depth of 22 km (of the best-fitting model), increasing the C1 resistivity value to 15 Ω m markedly increases the misfit on

most stations (excepted stations n05 and 203; Extended Data Fig. 7, top). Decreasing the C1 value to 1 Ω m increases the misfit at several sites across the area though the impact is less marked than the previously described increase in resistivity (Extended Data Fig. 7, bottom). This result indicates that the upper bound of resistivity is well defined, whereas the lower bound is constrained by only a limited number of sites. The model in Fig. 3 captures 'conservative', that is, maximum values of minimum resistivity, and thus, minimum melt fraction estimates.

Petrology

The magmas erupted on the Mayotte volcanic complex and on the recently active (2018–2021) submarine ridge define two different magmatic lineages (Fig. 2). Old magmas (10.6–1.9 Ma) from the southern Mayotte region are alkali rich and highly silica undersaturated[25] compared with their younger counterparts (0.75 Ma–present) from the north central–east domain and the most recent Holocene products[8,9] (including the 2018–2021 evolved basanite DR08 (red star) and the phonolite DR06 (yellow star) samples of this study). The latter are also silica-undersaturated, but show moderate alkali enrichment[8,9,25] (Fig. 2). In both cases, crystal fractionation is the main mechanism controlling magma evolution[7–9].

Extended Data Table 1 summarizes the petrological relationships between the three typical melt compositions recently discussed in the literature[7–9]. The bold numbers are used here to calculate the electrical conductivities of the C1 and C2 magmatic reservoirs in Fig. 4c,d.

Reference 8 modelled the production of the hydrous evolved basanite sample by crystallizing 50% (40% clinopyroxene, 10% olivine) of a parental basanite at temperatures of 1,090–1,050 °C and depths ≥37 km. Reference 7 experimentally demonstrated that phonolitic liquids containing up to 3.5 ± 5 wt% H_2O and with a similar composition to those found at Mayotte can be produced by the partial crystallization of the evolved basanite at 950–925 °C, depth of 6–8 km. This involves the crystallization of an olivine, plagioclase, amphibole, clinopyroxene, biotite, magnetite, ilmenite and apatite assemblage. The above petrological constraints define two distinct magmatic scenarios that are then used to interpret the nature of the electrical anomalies measured beneath Mayotte.

Considering the high sensitivity of electrical conductivity of magma on temperature, we performed crystallization experiments at 1,050–1,075–1,100 °C and 400–650 MPa (Extended Data Fig. 8) using internally heated pressure vessel apparatus[7] and piston cylinder apparatus[41] at Institut des Sciences de la Terre d'Orléans (ISTO). H_2O was varied between 0 and 3 wt% in the capsules to cover the water contents estimated in the natural samples (Extended Data Table 2). Scanning electron microscopy inspection of the experimental charges (Extended Data Table 2) revealed a mostly glassy sample with coexisting magnetite, ±olivine, ±clinopyroxene (Px) and ±plagioclase (Pl). At water contents characteristic of the natural evolved basanite, DR08, a temperature of 1,075 °C is near liquidus, with olivine–magnetite–glass assemblages similar to that analysed in DR08[8] (Extended Data Fig. 8). This is broadly consistent with the estimates of ref. 8, 1,095 ± 20 °C, based on olivine-melt equilibria.

Regarding the pressure conditions, Extended Data Fig. 8 indicates that DR08 paragenesis (olivine + magnetite + liquid) can form at 400–650 MPa for the range of water contents suggested in Extended Data Table 1.

Laboratory measurements of electrical conductivity and their modelling

All data and the model we fitted are available in an excel file entitled 'Laboratory data and models for Wawrzyniak et al' (see 'Data availability').

We used the experimental protocol first described in ref. 41 and adapted to silicate melts in ref. 4. Both dry and hydrated glassy samples were placed in 3/4-inch assemblages in a piston cylinder at ISTO. In a coaxial geometry[53], samples were sandwiched between an internal and external electrode composed of platinum[41]. Iron loss to the platinum capsule was found to be negligible given the short run duration (maximum 2 hours). These electrodes are connected to a Solartron 1260 impedance analyser using a four-wire connection, implying that no correction is required for the measured resistances, unlike for other protocols[54,55]. Temperature cycles were conducted to ensure the constancy and reproducibility of the temperature–conductivity paths. Experiments were conducted in the pressure and temperature ranges indicated in Extended Data Table 3. Experiments were stopped by switching off the power supply to the graphite furnace, yielding cooling rates >100 °C per second. All recovered samples were glassy.

The starting materials were prepared in the laboratory and consisted of ground samples of DR06 and DR08[7,9], which were dredged during the MAYOBS2 survey deep-sea sampling missions[43]. An excel file (see 'Data availability') provides the bulk compositions of these starting materials and all results. Extended Data Table 3 provides here a summary. These samples are glassy and they naturally contain dissolved H_2O (samples DR06- and DR08-). Dry samples of DR06 and DR08 were prepared by melting the glass powder in a high-temperature furnace in air (labelled DR08-0 and DR06-0). One H_2O-rich glass (DR06-6) was obtained from DR06 upon hydration at 1,100 °C and 250 MPa over 24 h in a pressure vessel at ISTO (for example, see refs. 4,56 for a similar procedure). Water contents of all glassy materials before the conductivity measurements were measured using an elemental analyser[4,41]. After conductivity measurements, we used infrared spectroscopy to determine the dissolved H_2O contents in glasses using the 3,600 cm^{-1} absorption band[56].

In addition, the water content of the DR08-' run was check using Raman spectroscopy techniques[57] at ISTO, and the obtained peak ratios compared with those derived from basanite standard glasses with known H_2O concentrations[58]. This yielded a water content of 3 ± 0.8 wt% for this experiment.

The conductivity data (σ in S m^{-1}) are all available in the excel file (see 'Data availability'). These data were regressed using an Arrhenius formalism against temperature and pressure. This involves the following equation with a pre-exponential term ($\sigma°$), an activation energy (E_a) and an activation volume (dV), defining the temperature (T, K) and pressure (P, bar) dependences:

$$\ln\sigma = \ln\sigma° - (E_a + P \times dV)/(R \times T) \quad (1)$$

These regressed parameters for each experiment (Extended Data Table 3) are relatively close to the parameters obtained by ref. 54 on an iron-free basaltic composition, and are much lower than the conductivity values recently obtained for alkali-rich nephelenite melt compositions[55].

The dependences of the electrical conductivity (σ, S m^{-1}) on melt water content (wt% H_2O), pressure (P in bar) and temperature (T in K) for each composition (DR06 and DR08) were all regressed to produce the following equations (2) and (3):

DR06-phonolite:

$$\ln\sigma = 7.56 + (-65,184 + \ln[H_2O\ \text{wt\%}] \times 3,367.2)/(8.314 \times T) + (0.0976 \times [H_2O\ \text{wt\%}] - 1.2688) \times P/(8.314 \times T) \quad (2)$$

DR08-evolved basanite:

$$\ln\sigma = 10.68 + (-113,332 + \ln[H_2O\ \text{wt\%}] \times 4,648.7)/(8.314 \times T) + (-0.70 \times P)/(8.314 \times T) \quad (3)$$

It is noted that we were not able to resolve a dependence of the pressure effect on water content for DR08. Equations (2) and (3) can reproduce the experimental data within 5% (in conductivity units, S m^{-1}). Equations (2) and (3) are used to draw the conductivity curves in Fig. 4

and the excel file (see 'Data availability') contains all the equations allowing these calculations to be done.

The effect of crystal content on the melt conductivity (Fig. 4c,d) was calculated using ref. 59. This empirical law calculates a crystal effect similar to the Hashin–Strickmann upper bound at high melt fraction (that is, $f > 0.5$) and evolves towards a tubule law for small melt fraction ($f < 0.1$). This is consistent with the methodology and the results of previous assessment of melt fraction in mantle domains from MT data[60] and imaged melt-crystal topology versus melt fraction[61,62].

The conductivity of crystalline phases is assumed to be in the range 0.01–0.001 S m^{-1} for the phonolite case (DR06; Fig. 4c). This range is assumed based on the low conductivity of the solid assemblage composed of olivine, plagioclase, amphibole, clinopyroxene, biotite, magnetite, ilmenite and apatite at 925–950 °C, given that the magnetite volume fraction in the solid is much less than 10%. We conducted various sensitivity tests showing that the conductivity of the solid (in the 0.01–0.001 S m^{-1} range) has a negligible impact on the calculated conductivity of C2. For the evolved basanite case (DR08; Fig. 4d), the crystallizing phases during the parental basanite to evolved basanite fractionation produces clinopyroxene and olivine in a 4/1 ratio[8]. We used refs. 63,64 to compute the conductivity of olivine and clinopyroxene as a function of temperature and water contents, respectively. To retrieve the olivine and clinopyroxene water contents, we used the basanite–clinopyroxene partitioning data of ref. 65 to calculate the H_2O content of clinopyroxene ($D^{CPX/melt} = 0.011$) and the equilibrium olivine–H_2O content was obtained after ref. 66 ($D^{CPX/melt} = 0.002$). All calculations and equations used to build Fig. 4c,d are available in the excel file (see 'Data availability'). The conductivity of the solid assemblages is shown in Fig. 4.

Data availability

The MT data used to build Fig. 3 and Extended Data Figs. 2–5 and laboratory data and model used to build Fig. 4 are available at the Cupidon data storage service of the BRGM: https://doi.org/10.18144/605e087b-74a7-4c3b-b733-a5e6167bea0a (ref. 45).

Code availability

Minim3d, the code used for the inversion of the MT data is a proprietary patented 3D MT inversion software from the IMAGIR private limited company (https://www.imagir.eu/). Original versions were first published by ref. 48 and benchmarked at workshops[50].

44. Darnet, M., Wawrzyniak, P., Tarits, P., Hautot, S. & d'Eu, J.-F. Mapping the geometry of volcanic systems with magnetotelluric soundings: results from a land and marine magnetotelluric survey performed during the 2018–2019 Mayotte seismovolcanic crisis. *J. Volcanol. Geotherm. Res.* **406**, 107046 (2020).
45. Wawrzyniak, P. et al. Dataset deposit for Nature paper Magnetotelluric evidence for a melt-rich magmatic reservoir beneath Mayotte. *BRGM* https://doi.org/10.18144/605e087b-74a7-4c3b-b733-a5e6167bea0a (2025).
46. Chave, A. D. & Thomson, D. J. Bounded influence magnetotelluric response function estimation. *Geophys. J. Int.* **157**, 988–1006 (2004).
47. Smaï, F. & Wawrzyniak, P. Razorback, an open source Python library for robust processing of magnetotelluric data. *Front. Earth Sci.* **8**, 296 (2020).
48. Hautot, S. et al. Deep structure of the Baringo Rift Basin (central Kenya) from three-dimensional magnetotelluric imaging: implications for rift evolution. *J. Geophys. Res. Solid Earth* **105**, 23493–23518 (2000).
49. Hautot, S. et al. 3-D magnetotelluric inversion and model validation with gravity data for the investigation of flood basalts and associated volcanic rifted margins. *Geophys. J. Int.* **170**, 1418–1430 (2007).
50. Miensopust, M. P., Queralt, P., Jones, A. G. & 3D. MT modellers. Magnetotelluric 3-D inversion—a review of two successful workshops on forward and inversion code testing and comparison. *Geophys. J. Int.* **193**, 1216–1238 (2013).
51. Ars, J.-M. et al. Joint inversion of gravity and surface wave data constrained by magnetotelluric: application to deep geothermal exploration of crustal fault zone in felsic basement. *Geothermics* **80**, 56–68 (2019).
52. Booker, J. R. The magnetotelluric phase tensor: a critical review. *Surv. Geophys.* **35**, 7–40 (2014).
53. Caricchi, L., Gaillard, F., Mecklenburgh, J. & Le Trong, E. Experimental determination of electrical conductivity during deformation of melt-bearing olivine aggregates: Implications for electrical anisotropy in the oceanic low velocity zone. *Earth Planet. Sci. Lett.* **302**, 81–94 (2011).
54. Ni, H., Keppler, H. & Behrens, H. Electrical conductivity of hydrous basaltic melts: implications for partial melting in the upper mantle. *Contrib. Mineral. Petrol.* **162**, 637–650 (2011).
55. Guo, X. et al. Electrical conductivity of CO_2 and H_2O-bearing nephelinitic melt. *J. Geophys. Res. Solid Earth* **126**, e2020JB019569 (2021).
56. Iacono-Marziano, G., Morizet, Y., Le Trong, E. & Gaillard, F. New experimental data and semi-empirical parameterization of H_2O–CO_2 solubility in mafic melts. *Geochim. Cosmochim. Acta* **97**, 1–23 (2012).
57. Di Genova, D. et al. Effect of iron and nanolites on Raman spectra of volcanic glasses: a reassessment of existing strategies to estimate the water content. *Chem. Geol.* **475**, 76–86 (2017).
58. Jiménez-Mejías, M., Andújar, J., Scaillet, B. & Casillas, R. Experimental determination of H_2O and CO_2 solubilities of mafic alkaline magmas from Canary Islands. *C. R. Geosci.* **353**, 289–314 (2021).
59. Gaillard, F. & Marziano, G. I. Electrical conductivity of magma in the course of crystallization controlled by their residual liquid composition. *J. Geophys. Res. Solid Earth* **110**, 2004JB003282 (2005).
60. Blatter, D., Naif, S., Key, K. & Ray, A. A plume origin for hydrous melt at the lithosphere–asthenosphere boundary. *Nature* **604**, 491–494 (2022).
61. Miller, K. J., Zhu, W., Montési, L. G. & Gaetani, G. A. Experimental quantification of permeability of partially molten mantle rock. *Earth Planet. Sci. Lett.* **388**, 273–282 (2014).
62. Gardès, E., Laumonier, M., Massuyeau, M. & Gaillard, F. Unravelling partial melt distribution in the oceanic low velocity zone. *Earth Planet. Sci. Lett.* **540**, 116242 (2020).
63. Gardés, E., Gaillard, F. & Tarits, P. Toward a unified hydrous olivine electrical conductivity law. *Geochem. Geophys. Geosystems* **15**, 4984–5000 (2014).
64. Yang, X. et al. Effect of water on the electrical conductivity of lower crustal clinopyroxene. *J. Geophys. Res.* **116**, B04208 (2011).
65. Adam, J., Turner, M., Hauri, E. H. & Turner, S. Crystal/melt partitioning of water and other volatiles during the near-solidus melting of mantle peridotite: comparisons with non-volatile incompatible elements and implications for the generation of intraplate magmatism. *Am. Mineral.* **101**, 876–888 (2016).
66. Hirschmann, M. M., Tenner, T., Aubaud, C. & Withers, A. C. Dehydration melting of nominally anhydrous mantle: the primacy of partitioning. *Phys. Earth Planet. Inter.* **176**, 54–68 (2009).
67. GeoTools (Viridien Group, 2025).

Acknowledgements We thank the Mayotte branch of the Environment and Energy Management Agency (ADEME) and the General Directorate for Risk Prevention (DGPR) for financially supporting the geophysical work (ADEME for 2019 and DGPR for 2019–2020), the staff from the French Geological Survey (BRGM) office in Mayotte for providing logistical support during the MT survey, and the Réseau de Surveillance Volcanologique et Sismologique de Mayotte (REVOSIMA). Since June 2019, Mayotte seismo-volcanic activity is monitored by REVOSIMA and funded by the Ministry for Ecological Transition and Territorial Cohesion (MTECT), the Ministry of Higher Education and Research (MESR), the Ministry of the Interior and Overseas (MIOM), with the support of the French Ministry for Armed Forces (MINARM). We also thank the RSMA Mayotte (Régiment du service militaire adapté de Mayotte) for hosting the Headquarters of the 2020 MT Survey. The French Hydrographic Office (SHOM) provided the bathymetry used in the MT inversion. D.S. was supported by the ANR projects GASTON (ANR-18-CE31-0021) and GERESFAULT (ANR-19-CE05-0043-02). We thank A. Slodczyk for her help with the Raman spectroscopy apparatus. The laboratory part of this work was supported by the French INSU call (TELLUS) and by the MAGBRINES project (ANR-24-CE49-6543). P.W. is grateful to J. Zlotnicki for his contributions to MT imaging and monitoring of French volcanoes and thanks the people who made this work possible, including P. Toulhoat, K. B. Slimane, S. Jaffrot, F. Tronel, C. Muçig, M. Darnet, N. Zornette and J.-D. Barnichon. This project has received funding from the European Union's Horizon Europe research and innovation programme under grant agreement number 101166936 —GEOASTRONOMY.

Author contributions P.W. and F.G. designed the project and supervised the writing of the paper. P.W. did the onshore MT survey, data processing and MT coordination. S.W. and F.D. contributed to the onshore MT survey. P.T. and J.-F.D'E. did shallow marine MT acquisition and data processing and wrote the corresponding text. S.H. performed 3D MT inversion, sensitivity analysis and data processing and wrote the corresponding text. J.A. and S.G. performed experimental petrology laboratory measurements on DR08 samples and wrote the corresponding text. D.S., S.G. and F.G. performed experimental petrophysics laboratory measurements on DR08 and DR06 samples and F.G. wrote the corresponding text. L.A. produced an interpretative scheme of the Mayotte plumbing system and supervised the interpretation based on J.D.'s 3D paraview integration project. I.T. provided an up-to-date bibliographical selection and wrote the Mayotte's geological section. A.L. provided seismic data selection and projections along interpretative profiles.

Competing interests The authors declare no competing interests.

Additional information

Supplementary information The online version contains supplementary material available at https://doi.org/10.1038/s41586-025-09625-4.

Correspondence and requests for materials should be addressed to Pierre Wawrzyniak or Fabrice Gaillard.

Peer review information *Nature* thanks the anonymous reviewers for their contribution to the peer review of this work. Peer reviewer reports are available.

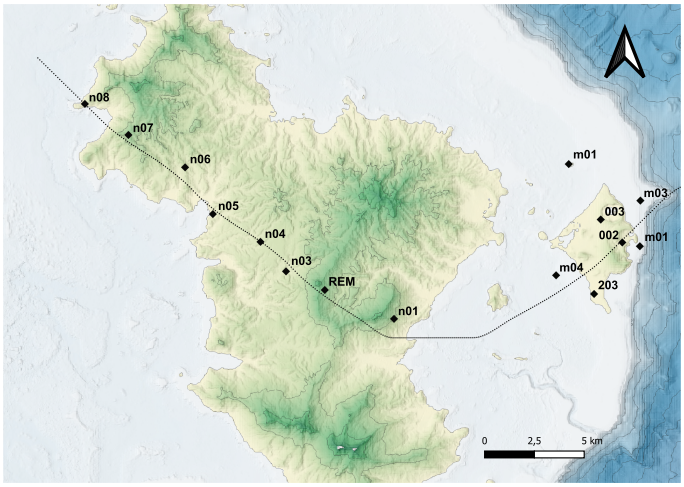

Extended Data Fig. 1 | Magnetotelluric (MT) station maps with names. Black diamonds: land and shallow marine MT stations. Stations REM, 002 and 203 are now permanent MT stations.

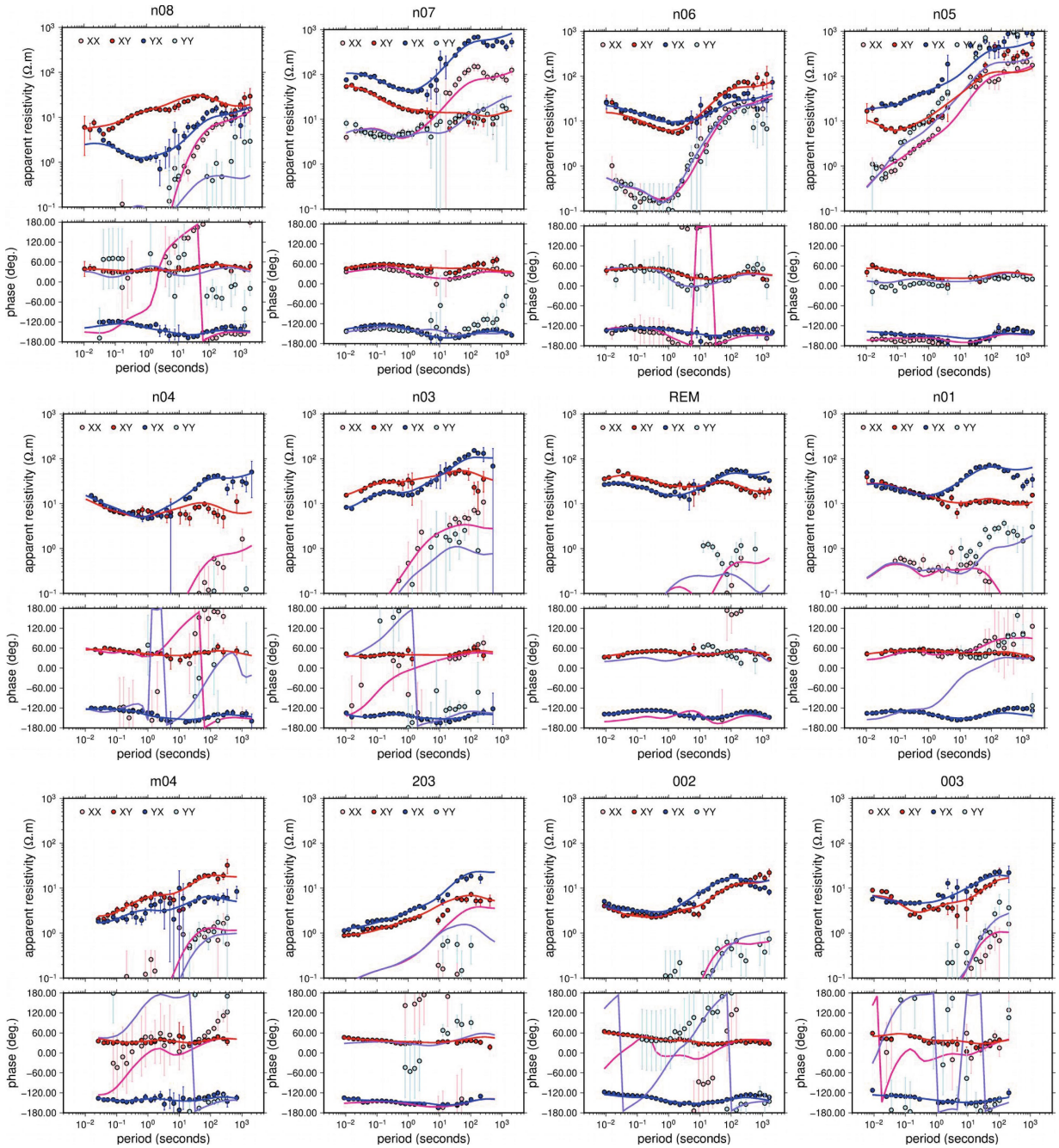

Extended Data Fig. 2 | Comparison of MT data and model inversion, part A. First array of MT soundings (dots) from west to east compared with modelled data from 3D inversion (lines). Sites 08, 07, 06, 05, 04, 03, REM, 01, m03, 203, 002, 003. Upper panels: apparent resistivity in Ω.m, Lower panels: phase in degrees. Sites labelled mxx are shallow marine MT site. All others are land MT sites (Fig. 1, Fig. 3 and Extended Data Fig. 1).

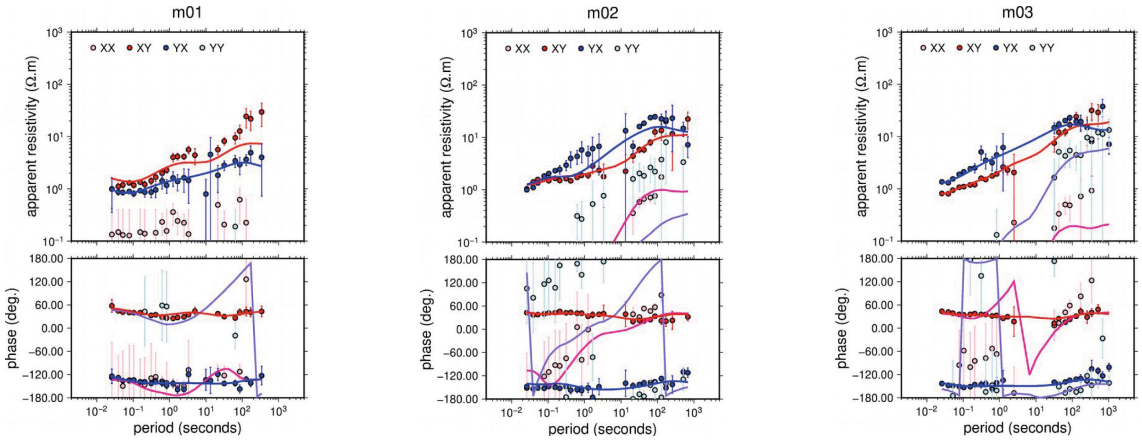

Extended Data Fig. 3 | Comparison of MT data and model inversion, part B. Second array of MT soundings (dots) from west to east compared with modelled data from 3D inversion (lines). Sites m01, m02, m03. Upper panels: apparent resistivity in Ω.m, Lower panels: phase in degrees.

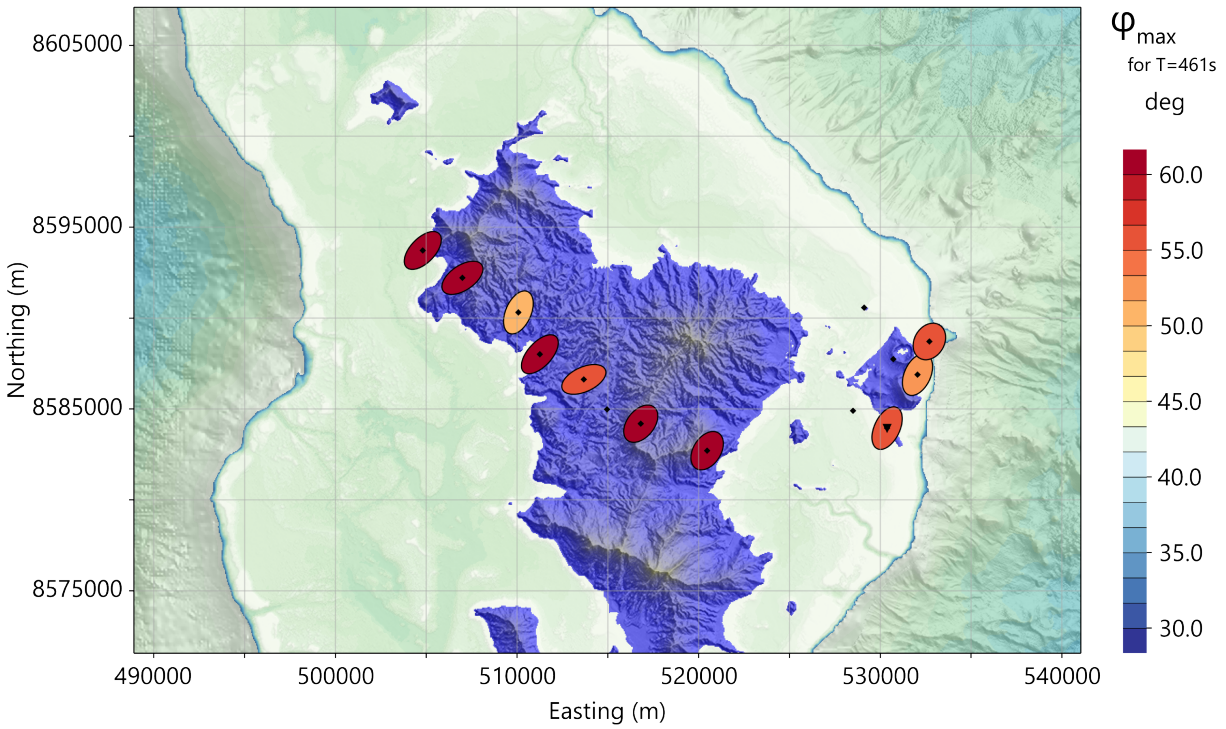

Extended Data Fig. 4 | Phase tensor map for each station of the MT survey at Mayotte. The Phase tensor map is obtained at a period of 461 s filled with φ_{max} values (all above 45°, indicating a resistivity decrease). We used the Geotools Software[67].

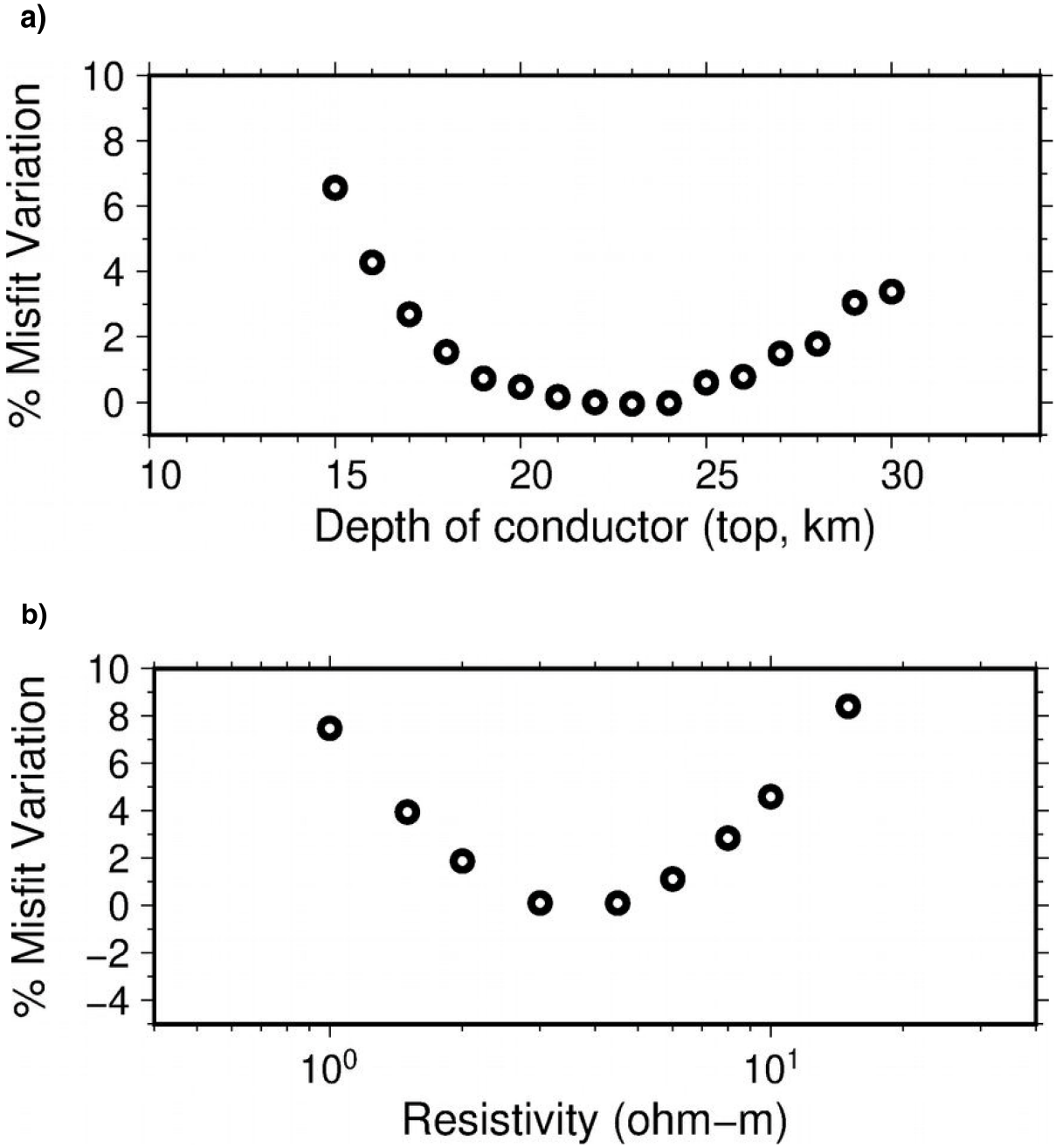

Extended Data Fig. 5 | Parametric sensitivity analysis performed on the C1 conductor. A) Misfit variation as a function of depth to top of C1, B) Misfit variation as a function of C1 resistivity.

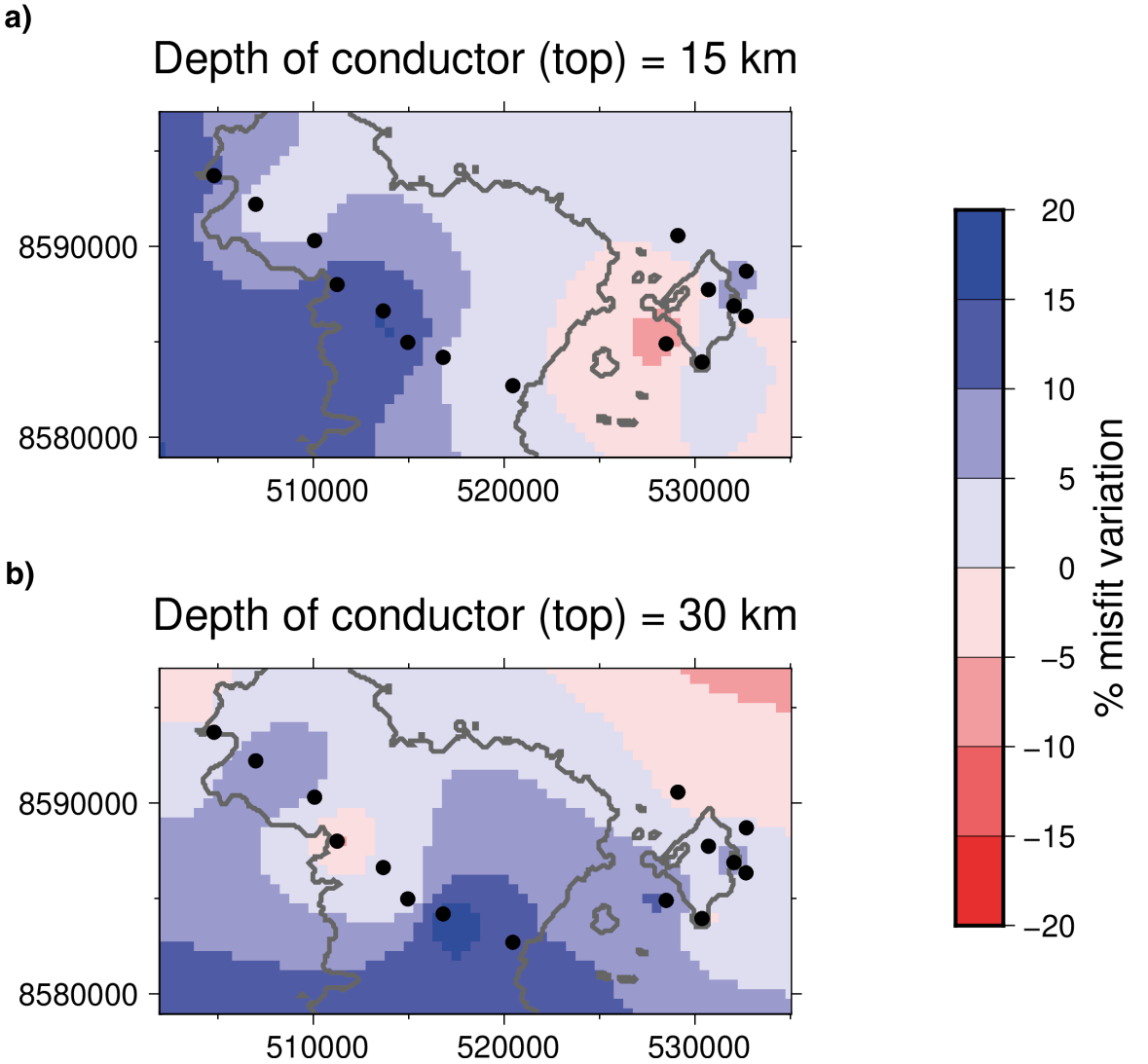

Extended Data Fig. 6 | Additional sensitivity analysis on the depth of the C1 conductor. We show the misfit variation map (in %) between best model (C1 at 22 km depth, shown on Fig. 3) and models obtained for minimum and maximum values of C1 depth, tested in sensitivity analysis and shown in Extended Data Fig. 5a, i.e. 15 and 30 km depth. The maps were calculated from misfit [(current model) -misfit (best model)]/misfit (best model) in % at all stations.

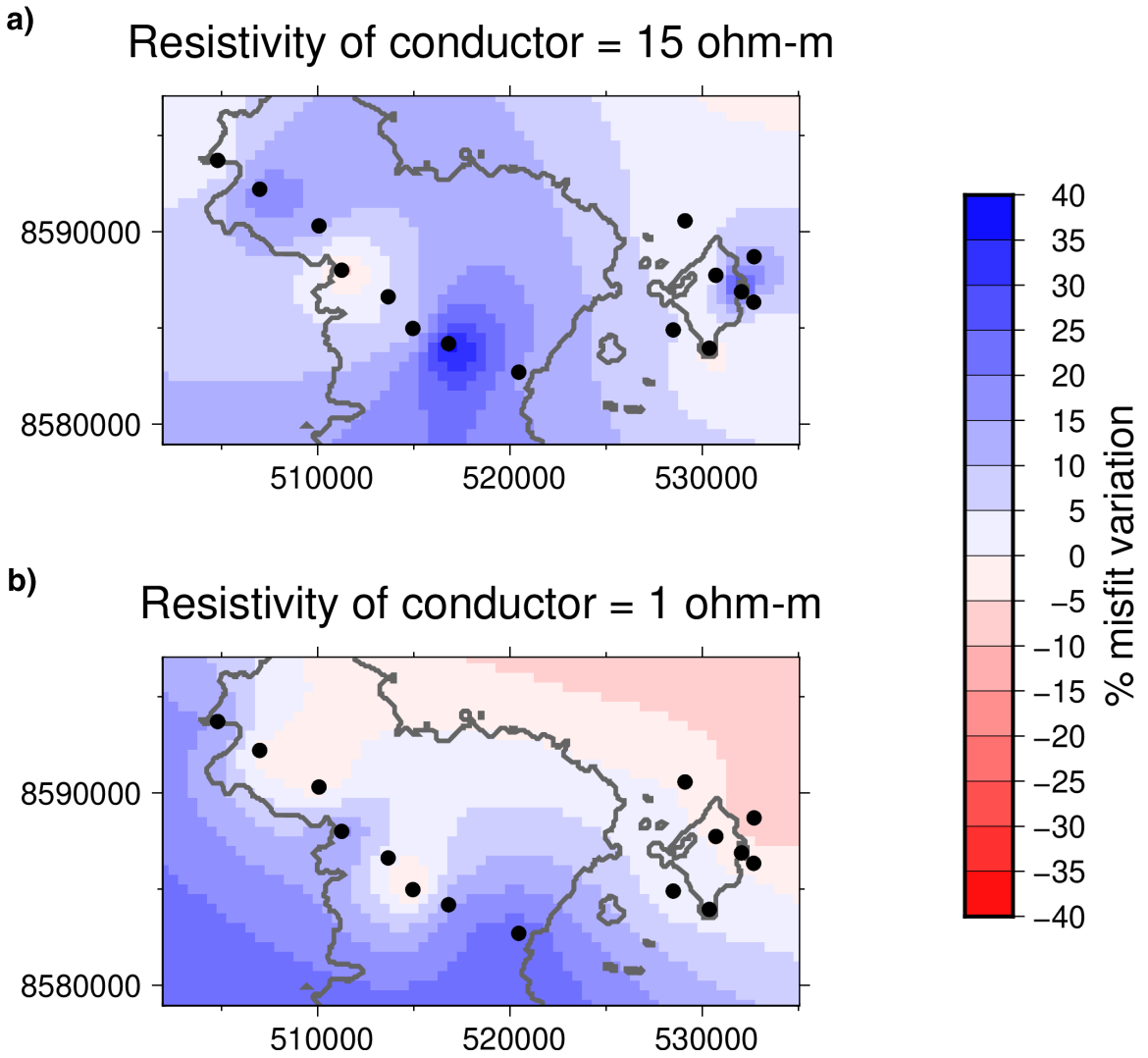

Extended Data Fig. 7 | Additional sensitivity analysis on the conductivity of the C1 conductor. We show the misfit variation map (in %) between best model (C1 at 22 km depth, shown on Fig. 3) and models obtained for minimum and maximum values of C1 resistivity, tested in sensitivity analysis and shown in Extended Data Fig. 5b, i.e. 1 and 15 ohm.m. The maps were calculated for misfit(current model)-misfit(best model))/misfit(best model) in %.

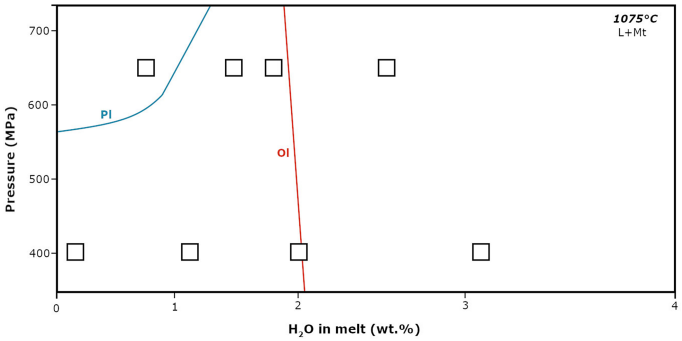

Extended Data Fig. 8 | Experimental constraints on the phase equilibria in Mayotte's evolved basanite. This plot illustrates the isothermal section at 1075 °C showing the mineral phases crystallizing on experiments conducted at 400 and 650 MPa and containing 0–3 wt.% H_2O. The H_2O contents correspond to water analysed in the melt using FTIR spectroscopy. Note that, below 2 wt.% water, Olivine (Ol) co-crystallizes along with magnetite (Mt). Olivine composition is Fo70, similar to that of the outer rim of the olivine crystals found in DR08[8]. Plagioclase (Pl) crystallizes at higher pressure on the water-poor part of the system. For melt water contents higher than 2 wt.%, the phase assemblage is liquid (L) and Mt.

Extended Data Table 1 | Types, properties and petrological relationships of Mayotte's magmas

Melt types	Water content (wt. %)	Temperature of formation (°C)	Depth of production (Km)	Depth of pre-eruptive storage (Km)	Produced from	Methods	References
Phonolite	3.5 ± 0.5	925-950	7 ±1	7 ±1	Evolved basanite + 65 % (± 10)	Exp. phase equilibria	Andujar et al. (2023)
	>~6	900-1000	15-20	15-20	Evolved basanite + 80% crystals	Xenolith analyzes + Calculated phase equilibria	Berthod et al. (2021b)
Evolved basanite	1.5 ±0.5	-	-		-	Exp. phase equilibria	Andujar et al. (2023)
	1.2-2.3	1095 ±20	37-48	17 ± 6	Parental basanite + 50% crystals	Raman analyses on Melt Inclusions Olivine-melt + CPX antecryst core Xenolith equilibration Crystallization model from Comoros Primitive Melts	Berthod et al. (2021a)
	1.73-1.9					FTIR analyses of glasses	This work
	1.8 ± 0.25	1075 ± 20	21 ±4	21 ±4	-	Exp. phase equilibria	This work
Parental basanite	1.15		80-100	-	Lherzolite melting	Back-crystallization models	Berthod et al. (2021a)

Names are identical to those used in the paper.

Extended Data Table 2 | Laboratory constraints on the phase equilibria in Mayotte's evolved basanite

Charge number	P (MPa)	H_2O wt%	Olivine	Magnetite	Plagioclase	CPX	Amp	Glass
T=1075 ± 5°C								
Dr08-C1	400	3.1		x				x
Dr08-C2	400	2.3	X	x				x
Dr08-C3	400	0.9	X	x				x
Dr08-C4	400	0.2	X	x				x
DR08-23	650	2.53		x				x
DR08-21	650	1.79	X	x				x
DR08-22	650	1.57	X	x				x
DR08-20	650	0.81	X	x	x			x
T=1050± 5°C								
DR08-19	650	2.33		x		x		x
DR08-18	650	1.88		x		x		x
DR08-17	650	0.93		x		x	x	x
DR08-16	650	b.d.		x		x		x
T=1100± 5°C								
DR08-27	650	2.97		x				x
DR08-26	650	2.09		x				x
DR08-25	650	0.98		x				x

Experimental run conditions and phase assemblages of the crystallization experiments at 1050–1100 °C, 400 and 650 MPa for oxygen fugacity conditions in the range FMQ-FMQ+1, are given. The bulk composition used (DR08) is provided in the file described in the Data statement availability statement.

Extended Data Table 3 | Summary of the laboratory conductivity measurements of Mayotte's melts

Sample	P bar	T°C	H_2O wt% Element. Analyzer		H_2O wt% FTIR		Electrical conductivity		
	Range	Range	Before	Range (>3 data)	After	Range (6 data)	ln s°	Ea	dV
DR8-0	7375-9375	1140-1432	0	n.d.	0.37	0.31-0.40	11.56 (0.2)	135292 (2670)	-
DR8-	6877-8875	1107-1309	1.73	1.67-1.9	2.18	1.98-2.53	10.64 (0.08)	114845 (3118)	-
DR08-'	8592-14764	1206-1380	1.73	1.67-1.9	n.d.		10.34 (0.03)	105459 (2806)	-0.61 (0.03)
DR6-0	7250-15625	1075-1246	0	n.d.	0.41	0.45-0.51	7.61 (0.26)	68848 (3238)	-1.25 (0.04)
DR6-	7625-15625	958-1187	1.69	1.43-1.67	1.33	1.17-1.49	7.59 (0.11)	64555 (1284)	-1.12 (0.018)
DR6-6	7250-15625	941-1160	6.57	6.49-6.65	6.35	6.19-7.18	7.53 (0.16)	58620 (1763)	-0.66 (0.02)

Experimental conditions, water contents (before and after conductivity measurements) and results of the conductivity measurements on samples DR06 and DR08 are provided. Conductivity unit is S/m, activation energy (Ea) is in J/mol and activation volume (dV) is in J/mol/bar.